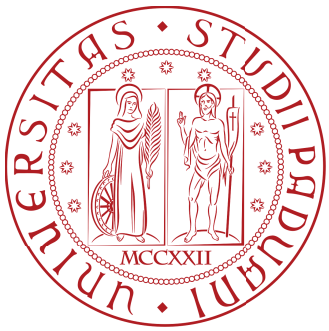

UNIVERSITÀ DEGLI STUDI DI PADOVA

Dipartimento di Fisica e Astronomia "Galileo Galilei"

Corso di Laurea in Fisica

Tesi di Laurea

Studio di contaminazione da polvere e relativo rumore da luce diffusa in rivelatori interferometrici per Onde Gravitazionali

Study of dust contamination and induced stray light noise in interferometric detectors of Gravitational Waves

Relatore

Dr.ssa Livia Conti

Correlatore

Dr. Andrea Moscatello

Laureando

Carlo Marchetto

Anno Accademico 2023/2024

Contents

Abstract

English Abstract

Stray light was one of the dominant sources of low-frequency noise during the previous O3 scientific run of Advanced LIGO (aLIGO) and Advanced Virgo (aVirgo), and it continues to be a major source of noise in the frequency band below a few hundred Hz. Dust particles deposited on the optical surfaces, together with the intrinsic roughness of the mirrors, can generate stray light. The Virgo group in Padua, of which I became a member on the occasion of the work reported here, is carrying out a systematic monitoring of cleanliness in different environments and laboratories at the Virgo site. As part of this larger project, the aim of this thesis is to implement a systematic procedure for the digital microscope provided, to analyse witness samples exposed at Virgo as part of the monitoring plan. This work will help to determine the level of cleanliness of the environments being monitored, allowing predictions to be made about the possible implications for Advanced Virgo and for future interferometers such as the Einstein Telescope.

Italian Abstract

La luce diffusa è stata una delle principali fonti di rumore a bassa frequenza durante la precedente campagna di acquisizione (O3) di Advanced LIGO (aLIGO) e Advanced Virgo (aVirgo), e continua a essere una fonte importante di rumore nella banda di frequenza al di sotto di qualche centinaio di Hz. In particolare, le particelle di polvere depositate sulle ottiche, insieme alla rugosità intrinseca degli specchi, possono generare luce diffusa. Il gruppo Virgo di Padova, di cui sono diventato membro in occasione del lavoro qui riportato, sta conducendo un monitoraggio continuo del livello di pulizia in diversi ambienti e laboratori del sito di Virgo. Come parte di questo progetto più ampio, l'obiettivo di questa tesi è implementare una procedura sistematica per il microscopio digitale fornito, per analizzare campioni di test esposti a Virgo nell'ambito del piano di monitoraggio. Questo lavoro aiuterà a determinare il livello di pulizia degli ambienti monitorati, permettendo di fare previsioni sulle possibili implicazioni per Advanced Virgo e per futuri interferometri come Einstein Telescope.

Chapter 1

GW Theory

The work reported in this thesis addresses some specific issues related to the assessment of cleanliness in different environments of the Virgo gravitational wave detector, important for estimating the stray light contributed by dust deposited on optical components. This chapter aims at giving an introduction to this work, first by offering an explanation of the physics of gravitational waves in section 1.1; section 1.2 is dedicated to the "main character" of GW detection: the GW interferometers; section 1.3 gives an overview of the noise sources that affect GW detection.

1.1 Gravitational Waves

In 1915 Albert Einstein proposed a new theory of gravity: the theory of General Relatity (GR). It is based on the fundamental and innovative idea of viewing gravity not as an instantaneous long-range interaction, but as a manifestation of the curvature of the space-time generated by mass and energy distributions.

In GR, space-time is mathematically defined as a 4-dimensional manifold described by the metric tensor $g_{\mu\nu}$, and its relation with mass-energy distributions is described by the famous Einstein Equation (EE):

$$R_{\mu\nu} - \frac{1}{2} g_{\mu\nu} R = \frac{8\pi G}{c^4} T_{\mu\nu}, \tag{1.1}$$

where $G = 6.67 \cdot 10^{-11} N \cdot m^2/kg^2$ is Newton's gravitational constant and $c = 2.99 \cdot 10^8 m/s$ is the speed of light; $T_{\mu\nu}$ is the energy-momentum tensor, $R_{\mu\nu}$ and R are Ricci's Tensor and Ricci's Scalar respectively.

This equation represents a set of 10 non-linear differential equations and these are generally difficult to solve analytically. However, it is possible to solve them by introducing a series of approximations.

First of all, the weak field approximation:

$$g_{\mu\nu} = \eta_{\mu\nu} + h_{\mu\nu}, \ |h_{\mu\nu}| \ll 1, \tag{1.2}$$

considering a flat space-time $\eta_{\mu\nu} = diag(-1, 1, 1, 1)$ with the addition of a small perturbative term, the derivatives of which are also small. Then, it is useful to define the trace reverse:

$$\bar{h}_{\mu\nu} = h_{\mu\nu} - \frac{1}{2}\eta_{\mu\nu}. \tag{1.3}$$

Introducing the Lorenz gauge: $\partial_\mu \bar{h}^{\mu\nu} = 0$, EE can be rewritten as:

$$\Box^2 \bar{h}^{\mu\nu} = -\frac{16\pi G}{c^4} T^{\mu\nu}, \tag{1.4}$$

In empty space there are no mass/energy distributions and the energy-momentum tensor is null so it becomes:

$$\Box^2 \bar{h}^{\mu\nu} = 0, \tag{1.5}$$

which has a set of plane-wave solutions of the form:

$$\bar{h}^{\mu\nu} = A^{\mu\nu} e^{ik_\rho x^\rho}. \tag{1.6}$$

Then, by introducing the Transverse Traceless gauge (TT gauge) and assuming the GW wave propagating in the z-direction ($\mu = 3$), the number of independent components of $A^{\mu\nu}$ is greatly reduced and $A^{\mu\nu}$ can be written as a linear combination of:

$$\epsilon^{+}_{\mu\nu} = \begin{pmatrix} 0 & 0 & 0 & 0 \\ 0 & 1 & 0 & 0 \\ 0 & 0 & -1 & 0 \\ 0 & 0 & 0 & 0 \end{pmatrix} \quad \epsilon^{\times}_{\mu\nu} = \begin{pmatrix} 0 & 0 & 0 & 0 \\ 0 & 0 & 1 & 0 \\ 0 & 1 & 0 & 0 \\ 0 & 0 & 0 & 0 \end{pmatrix}, \tag{1.7}$$

respectively "plus" and "cross" polarisation. The physical implication of this decomposition is that a GW travelling through z-axis will only affect the x and y components, and in general the GW effects are transverse to its propagation direction. The effect of a GW propagating with a direction perpendicular to a circle of masses in the xy plane can be described visually as shown in figure 1.1:

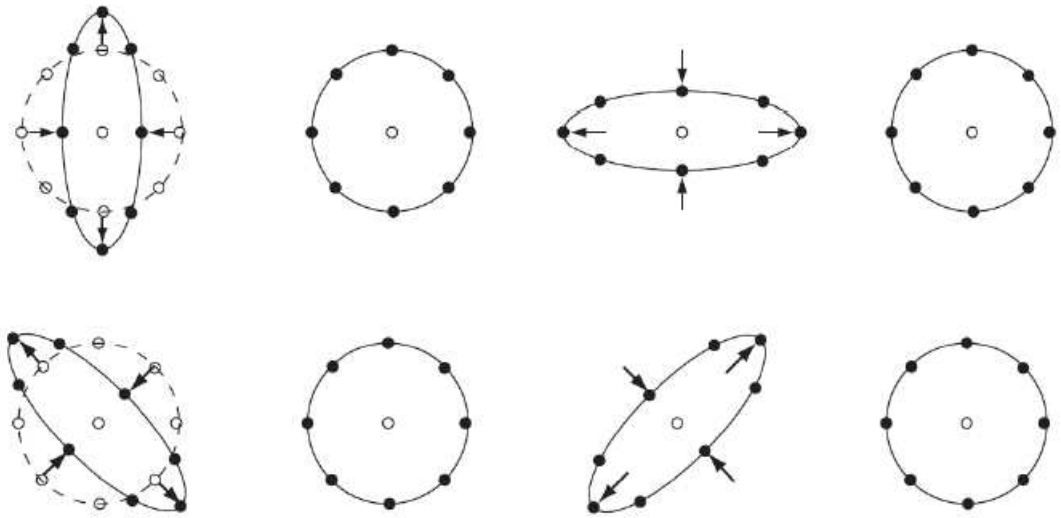

Figure 1.1: *GW effects on a set of masses distributed on a plane perpendicular to the GW propagation. Time is passing from left to right and the initial configuration of particles is shown by the open dots. Upper images refers to a GW incident in the figure plane with + polarizations, lower same GW but with × polarizations. Image from [12].*

This refers to the simplest case (empty space). In general $T^{\mu\nu} \neq 0$ and the wave equation becomes very complex to solve even in the easiest system (binary system): analytical solutions are available under certain assumptions, requiring numerical models and simulations to compute an accurate version of the waveform. However, its derivation is beyond the scope of this work.

1.2 Detection and Interferometers

Until a few years ago GW had never been directly detected, and only some indirect evidence has been found. In particular, in 1974 Hulse and Taylor observed a binary system of two neutron stars, one of which was a pulsar, and measured a variation in the rotational period compatible with the generation of a GW by the inspiral of the binary system. This earned them the Nobel Prize in 1993.

Only in 2015 the first GW signal was detected [2] thanks to LIGO (Laser Interferometer Gravitational-Wave Observatory), which consists of two interferometers located in Livingston, Louisiana, and Hanford, Washington. The detected signal is reported here:

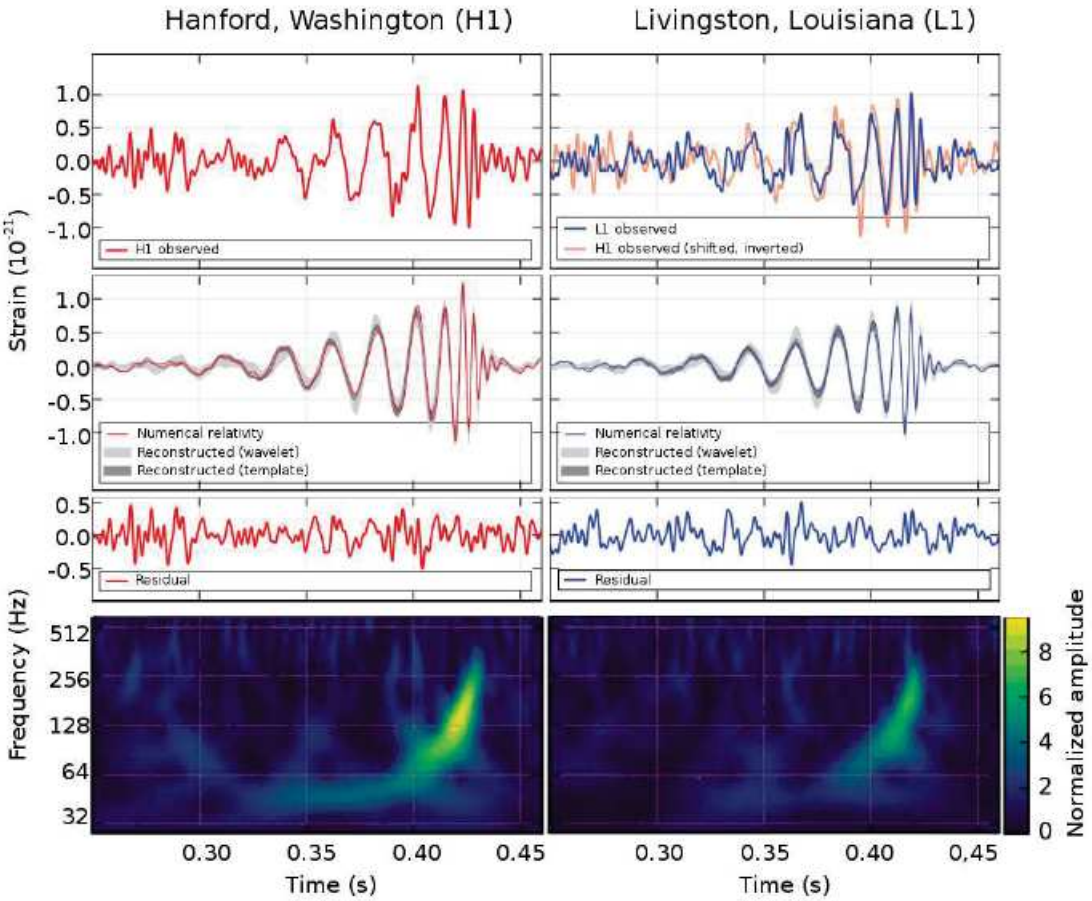

Figure 1.2: *The signal measured by the LIGO interferometer of the first gravitational wave ever observed GW150914. From top to bottom: the experimental data measured for the event, a numerical simulation of the waveform produced by a coalescence compatible with the observed event, residuals between data and simulation, and a time-frequency map of the signal. Image from [2].*

This detected signal originates from a Binary Black Hole (BBH) merger, where two BHs spiral closer and closer together, leading to a rotational frequency that increases with time reaching a maximum, together with the amplitude. After the merger, there is a settling phase of the resulting final BH, called "ringdown", which leads to an exponential decrease that causes the signal to rapidly disappear, as shown in figure 1.2. Analytically, the time dependence of the GW frequency f_{gw}, for a merging binary is [14]:

$$f_{gw}(\tau) = \frac{1}{\pi}\left(\frac{c^3}{GM_c}\right)^{5/8}\left(\frac{5}{256\tau}\right)^{3/8}, \tag{1.8}$$

where $\tau = t - t_{coal}$ is the time-to-coalescence parameter (t_{coal} being the time when the two body merge) and M_c is the chirp mass of the system, defined as:

$$M_c = \frac{(m_1 m_2)^{3/5}}{(m_1 + m_2)^{1/5}}. \tag{1.9}$$

It is important to note that the previous equations are valid under the quasi circular motion approximation, where the radius of the orbit remains relatively constant over a period. Therefore, these equations are applicable exclusively during the inspiral phase of the binary and before the coalescence.

To give an order of magnitude estimate for this frequency range in the case of GW150914: $m_1 = 36M_\odot$ and $m_2 = 29M_\odot$, assuming $\tau \approx 0.2s$ to avoid the late inspiral phase of the binary, it results $f_{gw} \approx$ 30Hz, a value that agrees with what can be observed in figure 1.2 at the beginning of the coalescence. For comparison, let us now look at one of the heaviest binary merger observed: GW190521 [1], which was formed by the merger of BHs with masses $m_1 = 85M_\odot$ and $m_2 = 66M_\odot$, keeping $\tau \approx 0.2s$, it results a frequency $f_{gw} \approx 20$Hz.

For the remaining part of this chapter, the focus is on how GWs can actually be observed. This is not a trivial task, given the frequency and hence the amplitudes to be revealed: $h \sim 10^{-21}m$. The fundamental consideration is that light travels at a constant speed c, and if the distance between two points is changed by the passage of a GW, as can be seen in figure 1.1, light would take a longer or shorter time to travel between the two points. This is the idea behind the use of interferometers (ITF) to detect GWs.

The basic system consists of three test masses: two of these masses are mirrors (M_x and M_y), while the third is a beamsplitter (BS). Each mass is suspended from a a series of pendula that isolates it from ground vibrations but allows it to swing freely in the horizontal direction. A laser (S) with a typical wavelength of $\lambda \sim 10^{-6}m$ is aimed at the beamsplitter. The beamsplitter splits the laser light into two beams directed down the arms of the interferometer. These beams are reflected by the mirrors M_x and M_y and then recombined at the beamsplitter on the "unused port" (the side not facing the laser or mirrors), and detected by the photodiode detector (PD). When the beams are recombined, they will interfere constructively if the lengths of the two arms, L_x and L_y, differ by $\Delta L = n\lambda$, and destructively if $\Delta L = (n + \frac{1}{2})\lambda$, where n is an integer. The system is arranged so that the beams interfere destructively if all three masses are perfectly stationary, and this is why it is said to work in the dark fringe configuration.

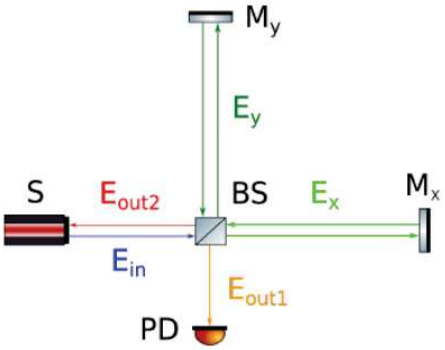

Figure 1.3: *Scheme of an interferometer for GW: M are the two mirrors, BS is the beam splitter, PD is the photodiode detector, and S is the laser source.*

Here is how an interferometer responds to the passage of a + polarised gravitational wave aligned with the two arms of the interferometer [23]. The GW has the following form:

$$h^{\mu\nu} = \begin{pmatrix} 0 & 0 & 0 & 0 \\ 0 & a & 0 & 0 \\ 0 & 0 & -a & 0 \\ 0 & 0 & 0 & 0 \end{pmatrix} \cos(\omega_{gr} t). \tag{1.10}$$

Defining $h_+(t) = a\cos(\omega_{gr}t)$ and considering a GW incident in the xy plane ($z = 0$), the infinitesimal distance in the Minkowski space becomes:

$$ds^2 = (-cdt)^2 + dx^2(1 + h_+(t)) + dy^2(1 - h_+(t)). \tag{1.11}$$

Then, for a light ray $ds = 0$, the time it takes for the light to travel from x=y=0 (BS) to the position of the mirror M_x placed at L_x is calculated as follows:

$$cdt = \pm dx(1 + h_+(t))^{\frac{1}{2}}, \tag{1.12}$$

By approximating at the first order it results:

$$dx \approx cdt\left(1 - \frac{h_+(t)}{2}\right), \tag{1.13}$$

and by integrating it:

$$\int_0^{L_x} dx = \int_{t_0}^{t_1} c\left(1 - \frac{h_+(t)}{2}\right) dt, \tag{1.14}$$

ans so:

$$L_x = c(t_1 - t_0) - c\int_{t_0}^{t_1} \frac{h_+(t)}{2} dt \approx c(t_1 - t_0) - c\int_{t_0}^{t_1 = \frac{L_x}{c} + t_0} \frac{h_+(t)}{2} dt. \tag{1.15}$$

The same behaviour is expected in the reverse direction:

$$\int_{L_x}^{0} dx = \int_{t_1}^{t_2} c\left(1 - \frac{h_+(t)}{2}\right) dt, \tag{1.16}$$

$$L_x = c(t_2 - t_1) - c\int_{t_1}^{t_2} \frac{h_+(t)}{2} dt \approx c(t_2 - t_1) - c\int_{t_1}^{t_2 = \frac{L_x}{c} + t_0} \frac{h_+(t)}{2} dt. \tag{1.17}$$

Summing the two equations and solving the two integrals yields:

$$2L_x = c(t_2 - t_0) - L_x \frac{\sin\left(\frac{\omega_{gr} L_x}{c}\right)}{\frac{\omega_{gr} L_x}{c}} h_+\left(t_0 + \frac{L_x}{c}\right), \tag{1.18}$$

and by inverting it:

$$\Delta t_x = t_2 - t_0 = \frac{2L_x}{c} + \frac{L_x}{c} \frac{\sin\left(\frac{\omega_{gr} L_x}{c}\right)}{\frac{\omega_{gr} L_x}{c}} h_+\left(t_0 + \frac{L_x}{c}\right). \tag{1.19}$$

Then, repeating the same procedure for L_y:

$$\Delta t_y = t_2 - t_0 = \frac{2L_y}{c} - \frac{L_y}{c}\frac{\sin\left(\frac{\omega_{gr}L_y}{c}\right)}{\frac{\omega_{gr}L_Y}{c}}h_+\left(t_0 + \frac{L_y}{c}\right). \tag{1.20}$$

In particular, the trend: $\sin(x)/x$ is typical of the interference figure.

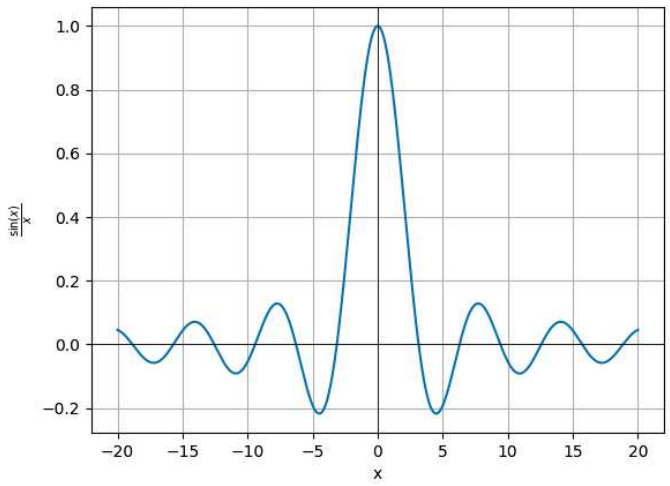

Figure 1.4: *Plot of the function* $sinc(x) = sin(x)/x$.

By varying L_x and L_y, the difference $\Delta t_y - \Delta t_x$ produces a phase variation of the form:

$$\Delta\phi = \omega_{laser}(\Delta t_y - \Delta t_x). \tag{1.21}$$

In particular with the approximation $L_x \approx L_y \approx L$, and introducing λ as the wavelenght of the laser:

$$\Delta\phi = \frac{4\pi}{\lambda}L \cdot h_+ \cdot \frac{\sin\left(\frac{\omega_{gr}L}{c}\right)}{\frac{\omega_{gr}L}{c}}. \tag{1.22}$$

The first factor may suggest arbitrarily increasing the lenght of the arms in order to maximize the effect, but the presence of the $\sin(x)/x$ function imposes a limit on it. By maximising the previous expression (using a GW frequency of 100Hz), an optimal length of approximately 750km can be found, a dimension that cannot be physically achieved on Earth. Therefore, an attempt is made to build interferometers with arms as long as possible. For example, the LIGO pair has arms reaching 4km while VIRGO has arms reaching 3km, which are still far from the optimal length.

To give an order of magnitude, assuming arm lengths $L = 3km$, a gravitational wave amplitude $h_+ \sim 10^{-21}m$, a frequency $f_{gr} = 100Hz$ and a typical laser wavelength $\lambda = 10^{-6}$ m; eq. 1.22 yields $\Delta\phi \sim 10^{-11}rad$, and thus $\Delta L \sim 10^{-18}m$. It should be noted that the fermi (fm), a typical unit of measurement for subatomic distances, is equal to $10^{-15}m$.

To solve this practical problem, there is a possible implementation in the ITF design: Fabry-Perrot Cavity.

Referring to the scheme in figure 1.3, an extra mirror is placed at the beginning of each arm, realizing an optical resonator known as the Fabry-Perot cavity. The light travels back and forth many times (order of 100) each arm before re-entering the beam splitter. This increases the effective distance travelled by the light by two order of magnitudes.

Another improvement is the power recycling configuration. This results from the fact that some of the light returning from the arms is sent back to the laser and is lost, and also interferes constructively on its way to the laser, which can damage the laser source. To mitigate this, a semi-reflective mirror (Power Recycling mirror, PR) is placed close to the BS on the way from the source to the BS, which also leads to an increase in the signal to noise ratio with respect to the 'shot noise' of the photons.

Modern ITFs 'recycle' also the gravitational wave signal: this is done by adding one more mirror after the beam-splitter, before detecting the interference pattern. This mirror is named the Signal Recycling mirror (SR).

Referring to the specific case of Advanced Virgo, its optical layout comprises two additional systems: the Input Mode Cleaner and the Quantum Noise Reduction. The first one is needed to improve the quality of the laser beam circulating the interferometer, in terms of beam pointing stability, spatial shape, frequency purity. The second is a complex system to reduce the noise due to the quantum nature of light, i.e. the radiation pressure noise and the shot noise.

Therefore, Advanced Virgo can be schematised as in the following figure:

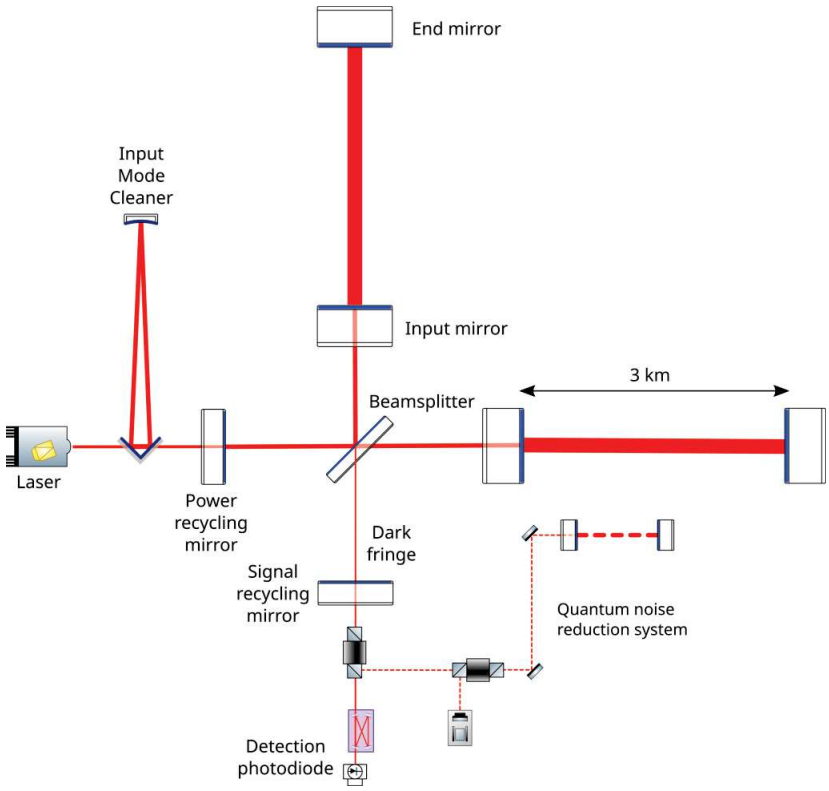

Figure 1.5: *Scheme of the Advanced Virgo ITF from [20].*

1.3 Noise Budget

The number of events and types of sources that GW interferometers can detect is determined by the instrument's strain sensitivity. The sensitivity is given as the total noise of the detector referred at the input, i.e. expressed in units of gravitational wave strain. Consequently, the characterization and minimization of all noise sources are primary tasks in the design and commissioning of the interferometer.

The effect of a noise source can be described by its Noise Spectral Density $S_x(f)$ as a function of the frequency, often referred to as the Power Spectral Density (PSD). This is typically converted into the Amplitude Spectral Density (ASD), denoted as $S_x^{1/2}(\omega)$, which has units of $1/\sqrt{Hz}$.

The overall performance of the systems constituting the interferometric apparatus is encapsulated in the sensitivity curve $S_x^{1/2}(\omega)$ of the instrument, as shown in the following figure.

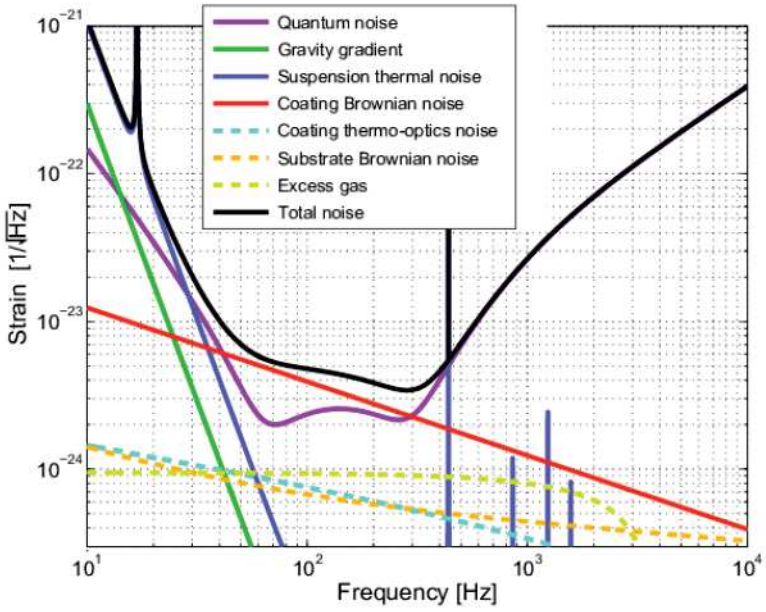

Figure 1.6: *Advanced Virgo sensitivity curve. Image from [19].*

There are many sources of noise:

- Quantum Noise: noise related to the quantum nature of light, it can be divided in two contributions:
  - Radiation Pressure Noise: caused by the impact of photons arriving at random times on the mirrors, it can limit sensitivity especially at low frequencies;
  - Shot Noise: related to the discrete nature of photons and the statistical fluctuations in the number of photons detected, it can limit the precision of the measurement from mid to high frequencies;
- Thermal Noise: all the noise due to random motion of matter components at finite temperature, it is given by two dominant contributions:
  - Coating Thermal Noise: vibrations of the atoms of the coating covering the surface of the mirrors, this affects the sensitivity especially at low frequency;
  - Suspension Thermal Noise: mechanical noise generated by the suspension system that holds the mirrors, it is very impactful at low frequencies;
- Seismic Noise: vibrations or movements in the Earth's crust can shake the mirrors and the optics of the inteferometer producing an unwanted signal, it is dominant at low frequencies;
- Gravity Noise: fluctuations in the local gravitational field due to variations in the Earth's density, atmospheric pressure variations or ground motion, it is relevant at low frequencies.

Chapter 2

Stray Light in Interferometers

In the phenomena of reflection or transmission of light, the term "stray light" refers to the portion of light that deviates from its intended path. In the specific case of GW interferometers, this effect becomes very relevant as the light scattered from the main beam can hit other surfaces, be reflected by them and then recombine with the main beam, leading to phase noise. In fact, the reflected light undergoes a phase shift modulated by the vibration of the affected surfaces, and these are generally not suspended, so there is great variability in the phase acquired. There is also a further source of noise in power due to the amount of stray light.

What hinders the identification of gravitational wave sources, especially at low frequencies ($< 100Hz$), is the presence of glitches in GW transients. In particular, during the secon part of the last observing run (O3b) at Ligo and Virgo, most of this glitches were generated by stray light. As reported in the GWTC-3 report [1], this type of noise appears as arcs in the time-frequency plane and, as shown in the spectograms 2.1, slow scattering noise produces long arcs (lasting 2.0–2.5 s), while fast scattering noise produces frequent short arcs (lasting 0.2–0.3 s).

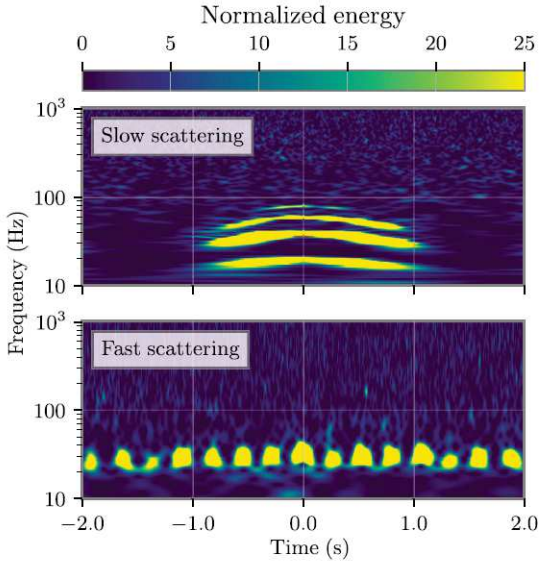

Figure 2.1: *Top panel: spectrogram of glitches caused by slow scattering. The multiple arches are due to multiple reflections between the test-mass optics and the scattering surface. Bottom panel: fast scattering. Image from [1].*

In this chapter, stray light caused by dust particles is discussed in Section 2.1. Section 2.2 covers dust particle deposition in clean environments, such as the different parts of GW ITFs. Section 2.3 provides an overview of the current monitoring plan implemented in Virgo.

2.1 Stray Light from Dust Particles

In the specific case of Virgo, the main sources of stray light include: surface roughness of the optics, dust contamination, scattering within the bulk material for transmissive optics and unstopped ghost beams (light generated by secondary reflections/transmissions, such as residual transmission in reflective mirrors or reflections in anti-reflective coatings). For the purpose of this study, only the contribution of dust will be discussed, as dust particles in the $0.1\mu m$ to $100\mu m$ diameter range can be the primary source of stray light.

The physical quantity of interest to quantify scattered light is the *Bidirectional Scattering Distribution Function* (BSDF). In order to understand its meaning some additional radiometric quantities must be introduced. First of all, the *radiant flux* is defined as the total electromagnetic energy ϵ transferred, emitted, or received per unit time t:

$$\Phi = \frac{d\epsilon}{dt}. \tag{2.1}$$

With this definition, *radiance* can now be expressed as the radiant flux emitted by a surface per unit solid angle $d\Omega$ and projected area of the source $dA\cos(\theta)$:

$$L(\theta) = \frac{d^2\Phi}{dA\cos(\theta)d\Omega}, \tag{2.2}$$

where θ is the angle between the normal to the emitting surface and the source-observer direction. Radiance measures the amount of light, or "brightness", a surface emits. It increases with the amount of flux emitted per unit area or per projected solid angle. One can also define the *irradiance* as the radiant flux received by a surface per unit area:

$$E = \frac{d\Phi}{dA}. \tag{2.3}$$

With these definitions, the BSDF can now be determined as the differential radiance of a scattering surface, normalized by the differential incident irradiance:

$$BSDF(\theta_i, \phi_i, \theta_s, \phi_s) = \frac{dL(\theta_i, \phi_i, \theta_s, \phi_s)}{dE(\theta_i, \phi_i, \theta_s, \phi_s)}, \tag{2.4}$$

where, in relation to figure 2.2, the couples $(\theta_i\ ;\ \phi_i)$ and $(\theta_s\ ;\ \phi_s)$ are the elevation and azimuth angles of the incident ray and of the scattered ray respectively. The idea is that when a surface is exposed to a certain irradiance, this irradiance influences the light emitted from the surface (i.e., radiance) through the scattering described by the BSDF. Thus, the BSDF completely describes how incident light on a surface is scattered and re-emitted in different directions.

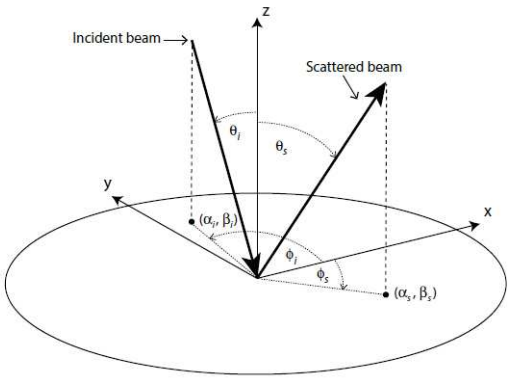

Figure 2.2: *Angles used in the definition of the bidirectional scattering distribution function. Image from [8].*

Turning now to the issue of scattering from dust particles, the problem becomes more intricate. Dust scattering is characterized by Mie Theory, a comprehensive and mathematically rigorous solution describing the scattering of an electromagnetic plane wave by a homogeneous sphere. In this model, dust particles are assumed to be spherical and dielectric. Their surface distribution is modeled with a function $f(D)$, and the particles produce both forward and backward scattering components.

A spherical and isotropic particle deposited on a surface is now considered, where R_f represents the surface reflectance. To compute the BSDF one fundamental assumptions is made: the radiation scattered in the forward direction reflects from the mirror and does not interact again with the particle. In this way the final BSDF comprises two contributions: the *Bidirectional Reflectance Distribution Function* (BRDF) and the *Bidirectional Transmission Distribution Function* (BTDF). The BRDF corresponds to the light that is reflected back either by the particle (backward-scattered beam) or by the surface (forward reflected-scattered beam). Conversely, the BTDF corresponds to the light that is transmitted by the surface. In this study, however, the contribution of the BTDF will be neglected and the BSDF will be made up entirely of the BRDF.

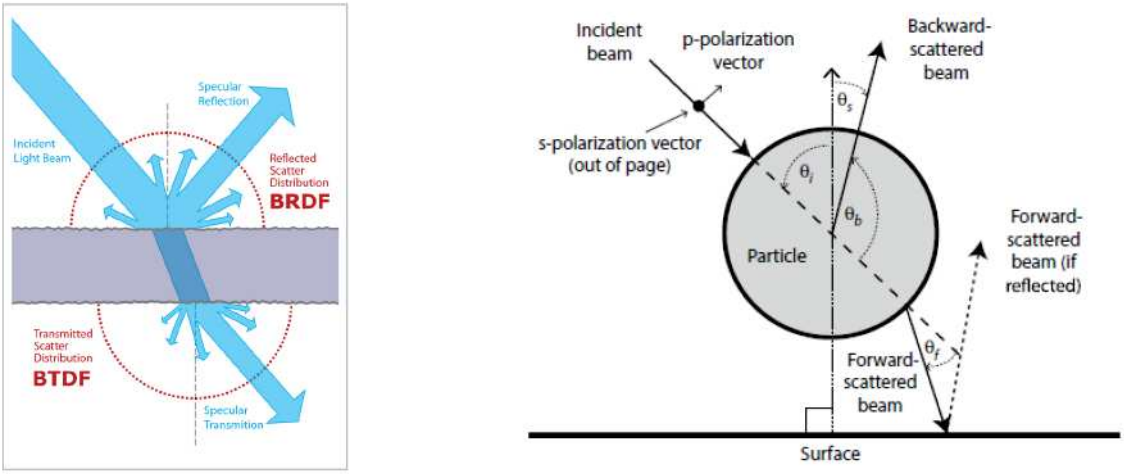

Figure 2.3: *Left: representation of the BRDF and BTDF contributions; the BSDF is the sum of the two (image from [22]). Right: geometry for Mie scattering of a particle on an optical surface. In this case, both the backward- and forward-scattered beams constitute the BRDF (image from [8].*

Assuming that the incident beam is unpolarized, the BSDF is calculated as [8]:

$$BSDF(\lambda, m, \theta_i, \theta_s) = \frac{1}{\left(\frac{2\pi}{\lambda}\right)^2 \cos(\theta_s)} \sum_D f(D) \cdot \left[\frac{R_f|S_1(x,m,\theta_f)|^2 + R_f|S_2(x,m,\theta_f)|^2 + |S_1(x,m,\theta_b)|^2 + |S_2(x,m,\theta_b)|^2}{2}\right], \quad (2.5)$$

where λ is the wavelength of light, θ_s is the scattering angle with respect to the surface normal, $f(D)$ is the particles density function and represents the number of particles with diameter D per unit area. The complex quantities $S_{1,2}$ are the Mie scattering matrix coefficients, where the indices 1 and 2 correspond to the perpendicular and parallel polarisations relative to the scattering plane, respectively. The quantity x is the size parameter, defined as $x = 2\pi R/\lambda$, where R is the radius of the particle. The variable m represents the complex refractive index of the dust material. θ_f and θ_b are the angles between the forward and backward scattered beams with respect to the direction of the incoming radiation. The summation is performed over each diameter D in the dust population.

2.2 Dust Particles Deposition in Clean Environments

The specific focus of this thesis centers on the deposition of dust particles in clean rooms. These are classified by ISO 14644-1 according to the airborne dust concentration and are divided into various ISO classes.

The parameter of interest for the classification is the volumetric concentration of particles with a diameter equal to or greater than D permitted in the environment: C_n, and it can be determined as [21]:

$$C_n = 10^{N_{ISO}} \left(\frac{0.1}{D}\right)^{2.08}, \quad (2.6)$$

where D is the diameter expressed in μm and N_{ISO} is the ISO class number, an integer number varying from 1 (the cleanest room: only 10 particles/m^3 with $D \geq 0.1\mu m$) to 9 (the dirtiest: order of magnitude of 10^7 particles/m^3 with $D \geq 0.5\mu m$) [13]. Examining equation 2.6, particles are expected to be significantly more numerous at smaller diameters, while fewer particles are found at larger diameters.

However, to study dust deposition on optics, it is not the volumetric concentration that is required, but the surface distribution of deposited particels and, more specifically, the cumulative surface distribution per unit area of particles with diameter $\geq D$.

This can be determined starting from the number of particles deposited as a function of the diameter $N(D)$, which can be calculated by knowing the particle deposition rate (PDR) and multiplying it by the exposure time t:

$$N(D) = PDR(D) \cdot t. \quad (2.7)$$

In turn, the deposition rate depends on the airborne concentration of D-diameter particles c_D and the deposition velocity of D-diameter particles v_D:

$$PDR(D) = c_D \cdot v_D. \quad (2.8)$$

Particle deposition is expected to be due to Brownian and turbulent motions, electrostatic attraction and most importantly gravity (at least for larger particles), so the deposition velocity is expected to be a function of particle size (D) and it can be calculated by Stokes settling equation.

In figure 2.4, a log - log representations of eq (2.6) for ISO 6 (solid line) and 7 (dashed line) is reported. The order of magnitude difference between the two can be seen and thus the ISO 6 is claener than the ISO 7.

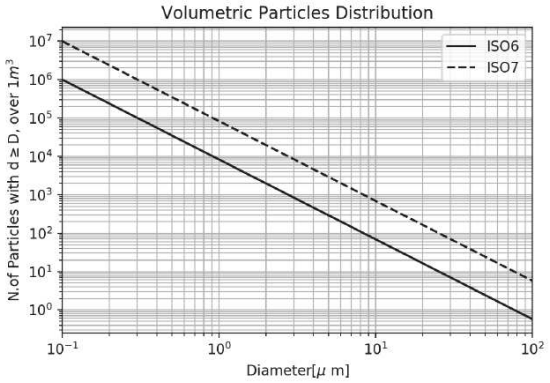

Figure 2.4: *log - log representations of the cumulative volumetric dust particles distribution, according to eq* (2.6)*. The solid and dashed lines refer to ISO6 and ISO7 classes respectively. Image from [9].*

2.3 Virgo Monitoring Plan

The challenge is then to find a way of counting how much dust actually deposit on the optics, so that the cleanliness of the environment can be monitored (to see if cleaning is needed) and the expected stray light from dust particles can be predicted. In this direction, a collaboration between the Padua and Genoa groups has started in 2020 for the continuous and systematic monitoring of specific in-air and in-vacuum environments in Virgo. As described in [15], since the optics cannot be removed for direct measurement, it was decided to use clean 3" silicon (Si) wafers as witness samples to the selected environments. In particular, the type of environment in which they are placed has a direct effect on the exposure time. In fact, in-air wafers have no particular restrictions and an exposure time of around one month has been set as a compromise between the number of clean samples available and the minimum time to obtain sufficient statistics. On the other hand, in-vacuum wafers are limited to the times when the sites are open, and therefore can have exposure times of many months or even more than a year. In addition, whenever external intervention is required, new wafers are placed at the beginning and end of such operations to investigate how much contamination they cause.

The wafers can be placed vertically (V) or horizontally (H): the former are more representative of the actual conditions being studied (dust on the optics) but accumulate less dust over time; the latter, on the other hand, are more susceptible to dust deposition due to the gravity and therefore allow for the collection of significant statistic even in the short term. Whenever possible, a pair of H/V wafers is placed in the same environment so that the ratio of the number of particles deposited on them can be studied. In this way, even where only H wafers can be arranged, the number of particles expected on a similar surface in the vertical direction can be reconstructed. In particular, the literature [6] suggests a value of 10% for the ratio $h = NoP_V/NoP_H$ (NoP_V and NoP_H being the number of particles deposited on a vertical and horizontal wafer, respectively). However, previous analyses of wafers of this type have found $h = 30\% \pm 10\%$ [15]. One aim of the current monitoring plan is therefore to further refine this estimate and compare it with the value expected from the literature.

Finally, it should be noted that these samples are mounted on specific holders that secure them in place throughout the exposure period. Each time a wafer is handled, specific tweezers are used to minimize the surface area in contact with external objects, thereby reducing the risk of unwanted contamination, as even the use of tweezers can leave dust particles or marks on the surface. Furthermore, when a wafer is removed, it is immediately placed in its plastic box, denoted with its location, orientation, and exposure time, and remains sealed until it is photographed (a procedure described in the next

chapter). During the photography phase, the samples are removed from the box (with tweezers) only for as long as necessary, then stored and sealed again.

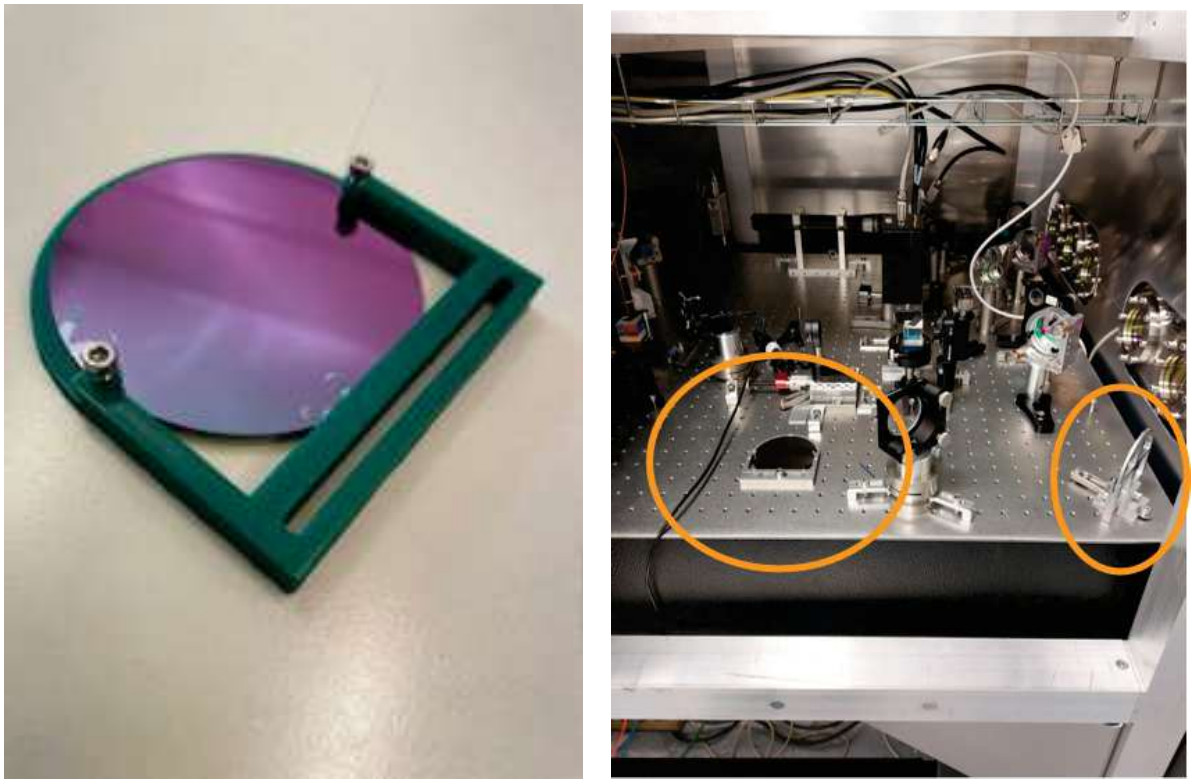

Figure 2.5: *Left: prototype of a holder used to secure the wafer during monitoring. The final holders are made of aluminium. Right: horizontal and vertical wafers placed in EDB (Environmental Detection Box) at Virgo's Detection Lab.*

Chapter 3

Experimental Measurements

Having presented the theoretical premises and the phenomenology, now the heart of the research work carried out is presented. Section 3.1 presents the instrumental apparatus used to photograph the wafers as part of the monitorin plan described in section 2.3. Section 3.2 describes the acquisition algorithm from the version in use at the beginnig of this work untill the latest version that includes improvements resulted from this thesis. The tests carried out in the preliminary calibration phase are also described. Finally, in section 3.3 the resulting analysis of two samples is reported.

3.1 Experimental Apparatus

The wafers are imaged using a digital microscope (Keyence VHX-7000) installed in an ISO-8 clean room in Padua. The instrument achieves an highest resolution of $0.3\mu m$ (determined by the refractive limit and maximum pixel resolution). The microscope stage can be adjusted along the x, y, and z axes, while the head is capable of vertical movement along the z axis. All thess movements have a resolution of $0.1\mu m$ and are programmable in C++. It is equipped with two different lenses, one fixed and one movable. The movable lens is equipped with two objectives that allow for a series of progressively higher magnifications: from $\times 20$ to $\times 100$ for the first and $\times 500$ to $\times 2500$ for the second. It has a 1/1.7-inch CMOS image capture sensor with 12.2 megapixels. The total pixel count is 4168 (horizontal) $\times$ 3062 (vertical), and the effective virtual pixel count is 4024×3036. Additionally, the microscope is equipped with its own analysis software and an autofocus function, which can vertically adjust within a certain z-range to focus on a specific feature within the observed area. The magnification levels and their corresponding image dimensions and fields of view are summarised in the following table:

zoom	$h[\mu m]$	$w[\mu m]$	$FoV[mm^2]$
$\times 20$	11318.4	15091.2	170.808
$\times 30$	7581.6	10108.8	76.641
$\times 40$	5637.6	7516.8	42.377
$\times 50$	4514.4	6019.2	27.173
$\times 80$	2808	3744	10.513
$\times 100$	2246.4	2995.2	6.728
$\times 500$	432	576	0.249
$\times 700$	324	432	0.140
$\times 1000$	216	288	0.062
$\times 1500$	151.2	201.6	0.030
$\times 2000$	108	144	0.016
$\times 2500$	86.4	115.2	0.010

Table 3.1: *In the table, different magnification levels are summarized with their corresponding image dimensions (height h and width w) and the field of view ($FoV = h \times w$).*

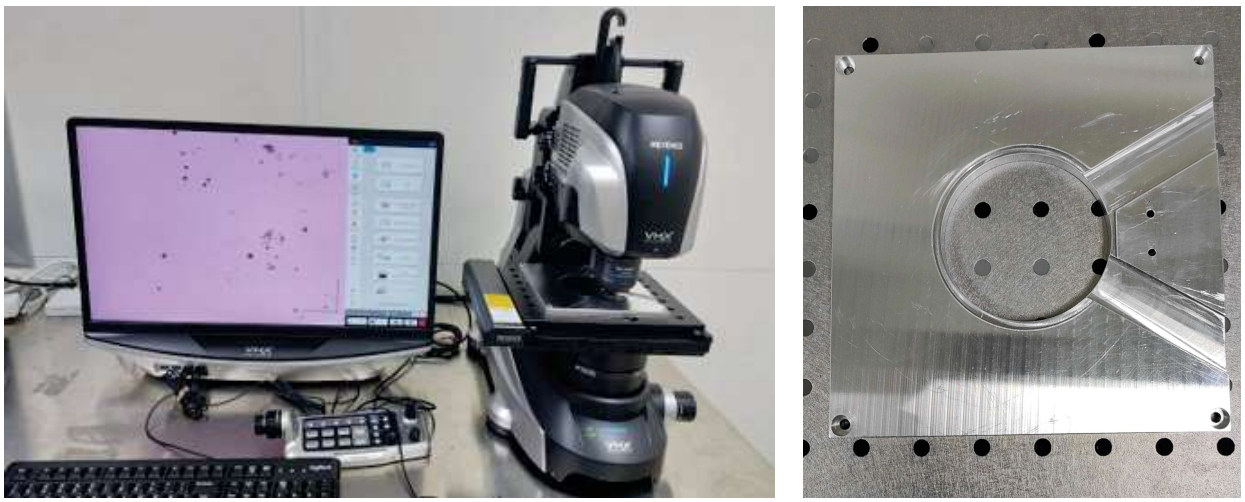

Figure 3.1: *On the left: photo of the VHX-7000 miscroscope used for the wafer imaging. On the right: photo of the holder (designed by M. Romanato, INFN-PD) used to fix the wafers during the photo acquisitions, the two recesses for the tweezers to pass through when placing and removing the sample are visible on the right.*

3.2 Acquisition Algorithm Tests and Refinement

The wafers consist of 3" diameter single and dounble sided polished crystalline silicon plates. When they are photographed, they are placed on an aluminium mask (figure 3.1), an holder to keep the sample stable during acquisition and to make its position repeatable for further measurements.

In the specific case of the analysis carried out for this work, photographs are taken at two magnifications:

- $\times 50$ magnification: this gives a larger field of view, but at a lower scale ($2.09 \mu m/pixel$). This is used for detecting larger particles ($D > 2\mu m$) and imaging a larger area;

- $\times 1500$ magnification: although it has a smaller field of view, it allows a higher scale ($0.07 \mu m/pixel$) to detect smaller particles ($D > 0.1\mu m$).

Due to the smaller FoV at the $\times 1500$ magnification, many photographs must be taken to cover the surface of the wafer. This can make the imaging phase and subsequent analysis very time consuming. Therefore, it is necessary to strike a compromise between the number of photographs taken and the time required, ensuring that the procedure is not too time-consuming, but allows for a sufficient statistics in the photographed area. Photos at $\times 50$ are taken in a 7×9 grid on the xy plane: for each field of view imaged at $\times 50$, 5 pictures are taken at $\times 1500$: one at the center of the $\times 50$ picture and then at the four corners. This choice excludes the portion of the wafer 1cm from the edge, to avoid any problem in the imaging due to the borders or introduced by the tweezers used to move and hold the wafer. Therefore, in total, for each wafer 63 photos are taken at $\times 50$ and 315 photos at $\times 1500$. As a result, the total area imaged is $1.71 \cdot 10^3 mm^2$ at $\times 50$ and $9.6 mm^2$ at $\times 1500$, out ogìf a total area of the sample of approximately $4.5 \cdot 10^3$. A pictorial representation of the grid of photos is reported in figure 3.2.

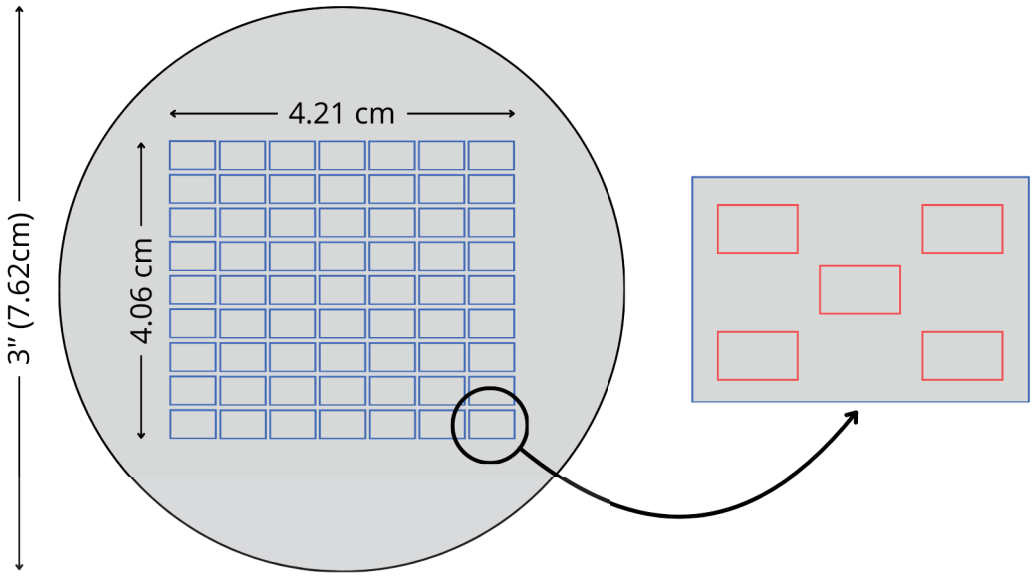

Figure 3.2: *The gray circle represents the 3" diameter silicon wafer. Overlaid on it is a grid diagram illustrating photos taken at* $\times 50$ *magnification (in blue), and zoomed-in detail of a cell showing the five photos taken at* $\times 1500$ *magnification (in red) for each cell. The size of the cells is not to scale.*

All photos are taken in bright field with an illumination source which is coaxial with the microscope objective. The whole procedure is automated and implemented using a C++ script.

One aspect that had to be calibrated was the focusing procedure of the algorithm to ensure that the photos were taken in focus. Firstly, it was observed that the depth of field at $\times 50$ (estimated at roughly $100\mu m$) is sufficient to optimize the focus once on a single particle of a wafer, ensuring all particles are in focus. Therefore, once focus is acquired, it is sufficient to capture pictures at the coordinates of the 7×9 grid. On the other hand, acquiring the focus only once per wafer is not possible at $\times 1500$ magnification. This is because the depth of field (estimated at roughly $1\mu m$) is inferior than the typical variations in the correct focus position across different particles on the wafer surface, likely due to residual non-planarity of the samples.

It is therefore necessary to find a way to move the microscope head at the proper position along the z axis for each picture. To minimize the time required for the focusing procedure, at the beginning of this thesis work, the following procedure was developed: eight particles located near the edge and evenly distributed around the circumference, along with one at the center, are manually identified by the operator. Let x_i, y_i denote their coordinates, where i ranges from 1 to 9. Autofocus is then conducted on all nine particles, determining their z_i positions. A quadratic fit with six parameters is then applied over the nine triplets (x_i, y_i, z_i) to define the surface representing the optimal focus. The fitting function used is as follows (eq 3.1), and in figure 3.3 an example of the performed fit of the surface is reported.

$$z = ax^2 + by^2 + cxy + dx + ey + f. \tag{3.1}$$

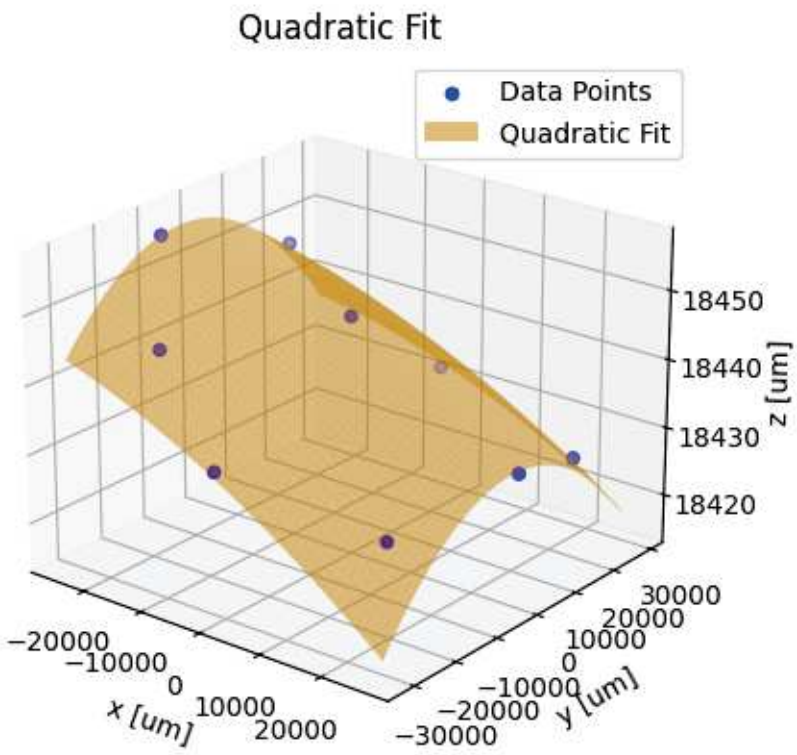

Figure 3.3: *An example of the quadratic fit performed over 9 points of (x_i, y_i, z_i) coordinates is shown. The residual curvature is depicted, highlighting variations on the order of 10-30 μm across the z positions of different points.*

In an initial phase, some preliminary work was conducted to test the procedure described above. However, a problem arose with the acquisition at $\times 1500$. Specifically, after identifying an object (such as a particle or a specific feature) to focus on, a code was implemented to use the autofocus function to measure the focus z position every 10 minutes for an arbitrary amount of time. It was observed that the optimal height z of the microscope head lowers with time, typically by about $10\mu m$ in about 2h. These variations in z would therefore affect future photo acquisitions (which take about 1 hour), as the initial focus fit (figure 3.3) may no longer accurately predict the optimal microscope head positions over time. This would result in out-of-focus images, if the procedure outlined above is followed. In order to understand, characterise and possibly resolve this effect, various tests were performed to track the z focus position as a function of time.

The following factors were specifically studied: the dependence on the weight applied to the microscope stage (holder + wafer), the impact of the focus sampling interval, the influence of head movement, the examination of multiple points on the surface, the effects of environmental parameters such as temperature, pressure, and humidity, and the implementation of a fixed delay before specific microscope operations.

3.2.1 Relaxation due to the weight carried by the plate

To study the dependence on the weight applied to the microscope stage and determine if it causes the lowering effect, the initial series of tests focused on details directly on the microscope stage, without the holder or a wafer mounted. An example of the focused feature is report in B. Looking at figure 3.4, significant fluctuations in measurements were observed, varying by more than $1\mu m$, with no clear downward or stable trend of the z positions identified. In fact, no distinct object on the plate

emerged from the background that could be effectively focused on. Consequently, the test did not yield conclusive results.

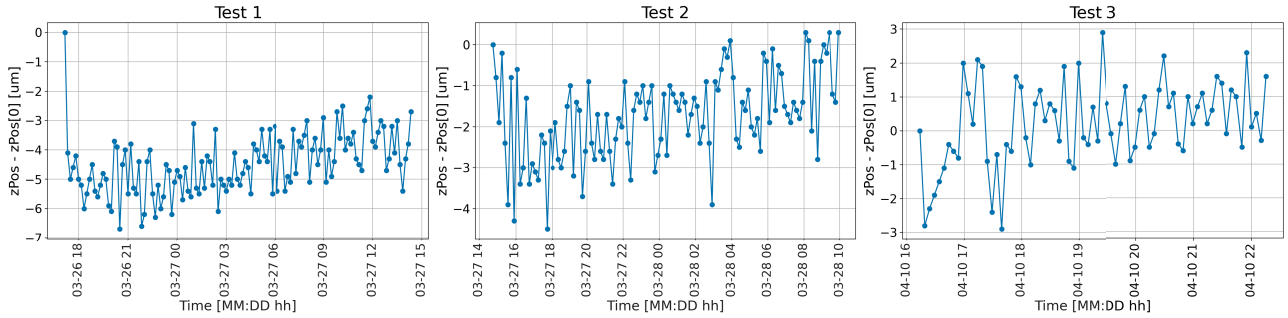

Figure 3.4: *Plots showing the change in focus over time relative to the initially found focus. The three tests were performed focusing directly on the empty microscope plate, the first two tests with a sampling interval of 10 min, and the third with 5 min.*

Then, only the holder was mounted and the measurements were repeated by focusing features on its surface. An example of the focused feature is report in appendix B. In this case (figure 3.5), the decrease in the z focus position can be appreciated, in particular it is observed a change by 5-10μm over approximately 1 hour, after which the focus position appears to stabilize reaching a constant value.

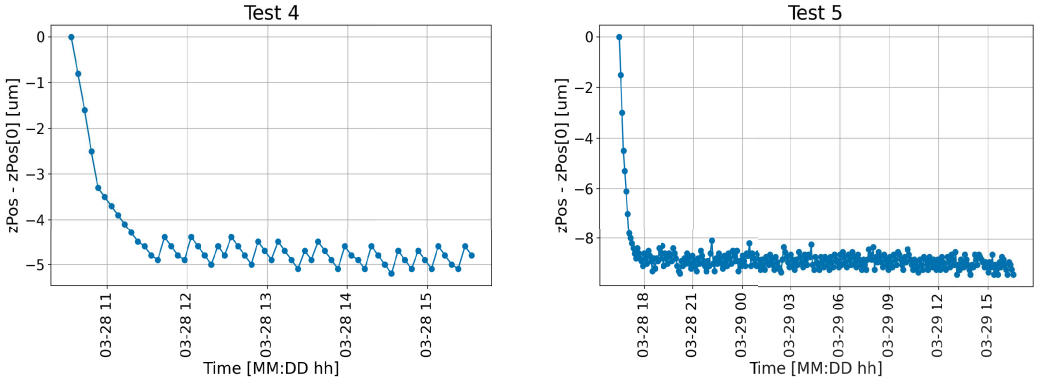

Figure 3.5: *Plots showing the change in focus over time relative to the initially found focus. These tests were performed focusing on a feature on the holder surface and both with a sampling interval of 5 min.*

3.2.2 Sampling interval dependence

A second test was performed to check if the 1h time scale of the decrease observed in figure 3.5 depends on the rate at which focus positions at $\times 1500$ are taken. In fact, during autofocus, the microscope head moves a bit along z until it focuses on the desired point, and a more or less frequent movement of the head may have an effect.

After selecting a specific point, focusing was repeated over time with sampling intervals of 2, 5, and 10 minutes, respectively. The results are shown in the figure 3.6, where it can be observed that the drift remains consistent, typically ranging between 5-10 μm within 2 hours. Therefore, a dependence on the sampling rate is excluded.

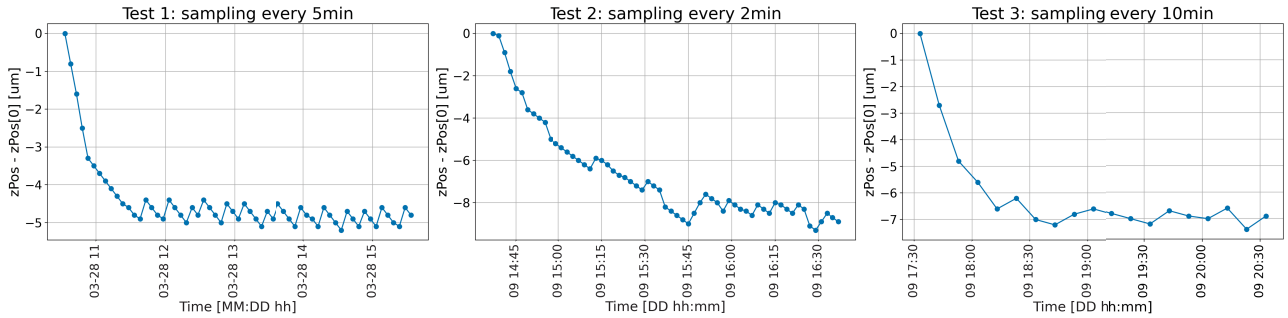

Figure 3.6: *Plots showing the change in focus over time relative to the initially found focus. These tests were performed by focusing on a feature on the holder surface, but varying the sampling interval: 5 min, 2 min, 10 min respectively.*

3.2.3 Moving away the head at every measure

At this point, and for all subsequent tests, a test wafer was also mounted on the holder to focus on particles on its surface.

On a few occasions during testing, the autofocus failed, losing particles and focusing on impurities on the lens, or simply going out of focus, with variations of hundreds of microns. In fact, if the target is very blurry when the autofocus starts, it may fail and move the head away, resulting in an out-of-focus image.

A new test was performed, aiming and veryfing if the decrease in focus position was due to excessive movements of the microscope's head. In particular, the head was moved $300\mu m$ away after each autofocus, returned to the previous z after 10 minutes and then a new autofocus was started. The result is reported in figure 3.7: here, a relaxation is observed that does not appear to reach saturation within the 16 hours of acquisition. However, this test was not pursued any further as it is far from the useful configuration for real acquisition.

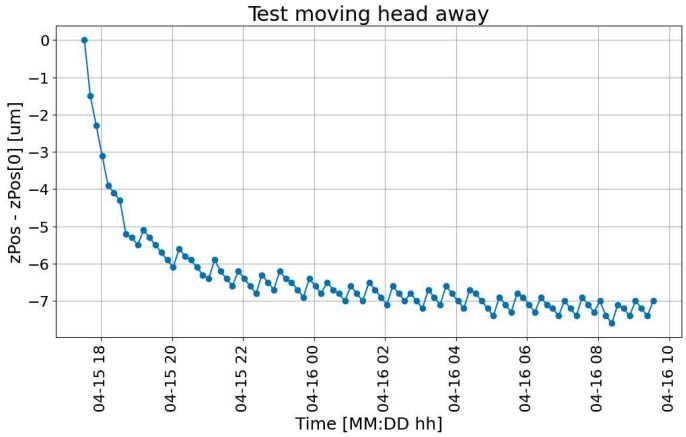

Figure 3.7: *Plot showing the change in focus over time relative to the initially found focus. This was done by focusing on a particle on the wafer and then moving the head away after each measurement.*

3.2.4 Multiple points and environmental control

Then, it was studied whether the lowering affects different points on the surface of the wafer in the same way. To do this, five different particles were selected for focusing: one in the central region and four along the edge of the wafer. Autofocus was performed on all five particles during each iteration, every 10 minutes. The results are shown in figure 3.8 and it can be observed that the five points decrease in the same way over time. The only difference between the two acquisitions reported is

the total duration. It must be noted that in the second acquisition there is a drop at about 10:40, a behaviour never observed before, but corrisponding to the start of scatterometer activity in the room.

In addition, these and subsequent tests are accompanied by monitoring of environmental parameters within the Clean Room. This is done by continuously acquiring the output of an environmental monitoring sensor that measures temperature, pressure, and humidity. The sensor is connected to a Raspberry Pi computer positioned near the microscope. Specifically, this setup is part of a PCTO project developed in Padua [11]. The aim is to test whether the deacrease could be compared with changes in these environmental parameters.

In particular looking at the temperature plots in figure 3.9, both show an initial drop, probably due to the fact that the opetators left the room, followed by a quasi constant phase and a subsequent increase in temperature. This increase may be attributed to the presence of operators in the laboratory during the final phase of the acquisitions. It is also important to note that the time scales of the environment parameters plots and the focus variation plot differ.

However, these tests are not conclusive and a correlation between relaxation and at least temperature cannot yet be ruled out. This should be investigated further by moving the sensor closer to the microscope to make it more sensitive to temperature changes in the instrument.

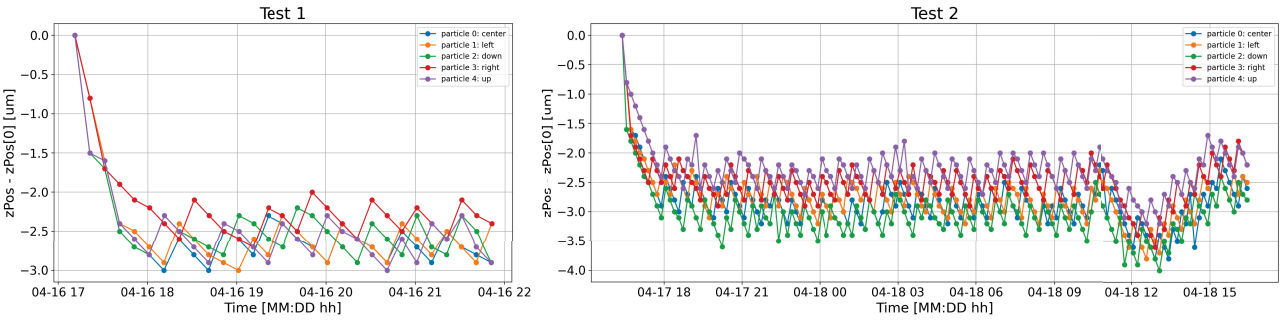

Figure 3.8: *Plots showing the change in focus over time relative to the initially found focus for 5 different points on the wafer. The main difference between the two acquisitions is the total duration.*

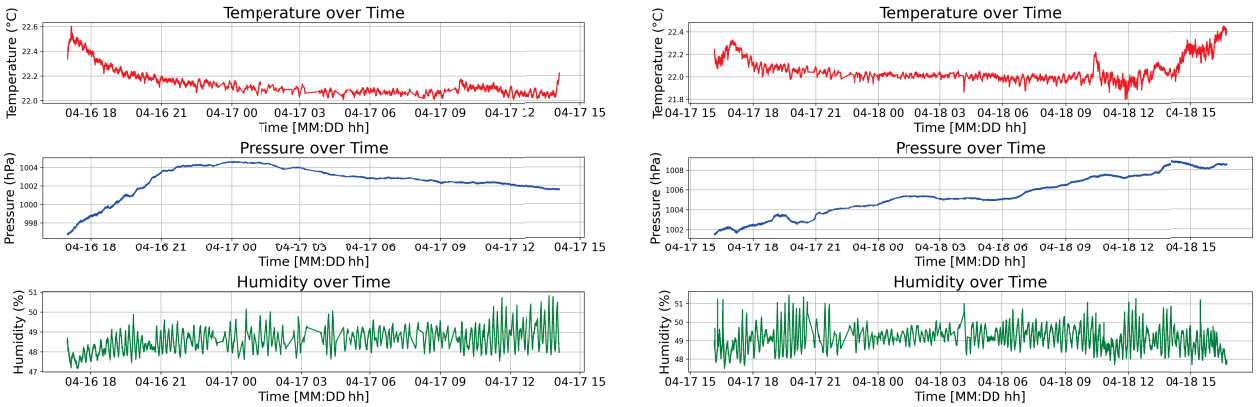

Figure 3.9: *Plots of temperature, pressure and humidity over time during the two acquisitions shown in figure 3.8: the first on the left and the second on the right. It is important to note that the time scale of these plots is different from that presented in figure 3.8.*

3.2.5 Waiting time

The tests conducted and presented so far do not allow to find a clear cause for the focus drift that can be eliminated to achieve stable focus. Therefore, it has been decided to take measurements after the drift has ceased and the focus has stabilized. In the following tests, the acquisition procedure was

implemented introducing a 2 hour delay at different points in the code to check two things: firstly, if this delay could be used to get rid of the problem, and secondly, to try to find out which microscope operation is causing the relaxation. Two tests were conducted with the delay set before connecting the microscope to the remote control interface on the PC, and two additional tests with the delay set immediately after connection, but before initializing the movement of the stage and adjusting the lighting settings.

As mentioned, the first test was conducted twice: the first time, no relaxation was observed (figure 3.10, top left), but this result was not reproducible, so it is not considered reliable. In fact, during the second attempt, the typical relaxation was observed. This consistent result was also obtained in both tests where the wait time was set after connecting the microscope to its remote control interface.

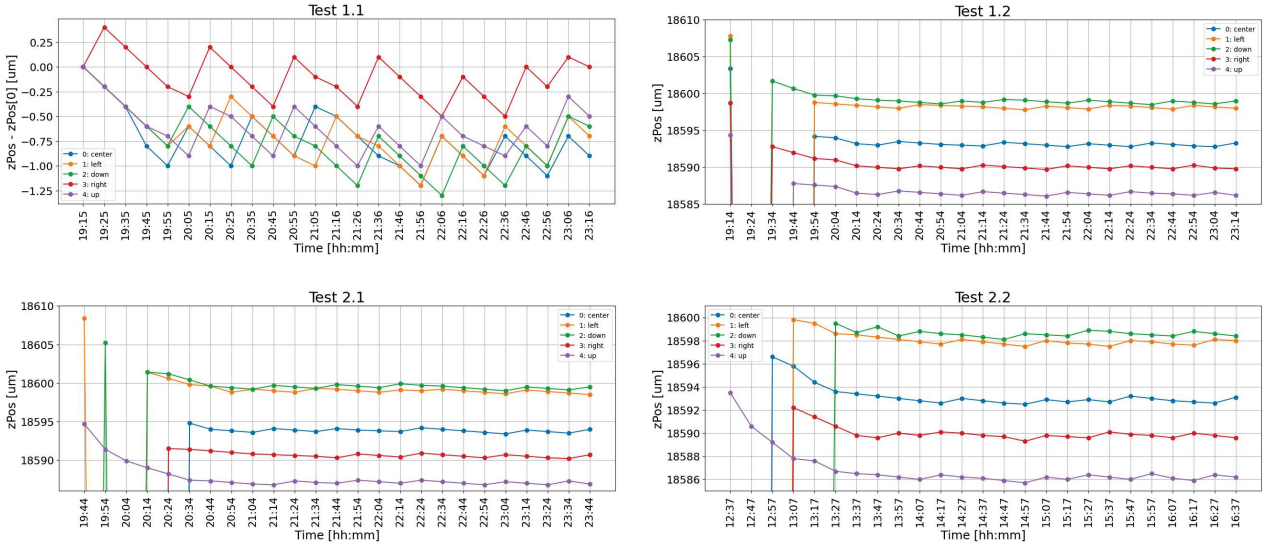

Figure 3.10: *Plots showing the change in focus over time relative to the initially found focus for 5 particles. The top two plots of the tests with the waiting time just before connecting the microscope to its remote control interface, the bottom two with the waiting time just after connection but before initialisating microscope settings.*

3.2.6 Mockup of a real acquisition procedure

Finally, a series of tests were carried out to test a new possible procedure of imaging of a Virgo wafer: first nine particles are found manually recordint their (x,y,z) positions, then the focus acquisition code is split into two stages:

- 2-3 hours with autofocus every 10-15 min on the nine particles (one in the centre and eight along the edges), updating the z focus positions and fitting them with a quadratic function (see figure 3.3) to be used to determine the nine z positions of the following iteration. In this way, the decrease is followed and corrected over time;

- 2-3 hours of moving the head on the same nine particles every 10-15 min and taking a photo of them. This allowed for checking whether the photos were in focus or not after completing the acquisition.

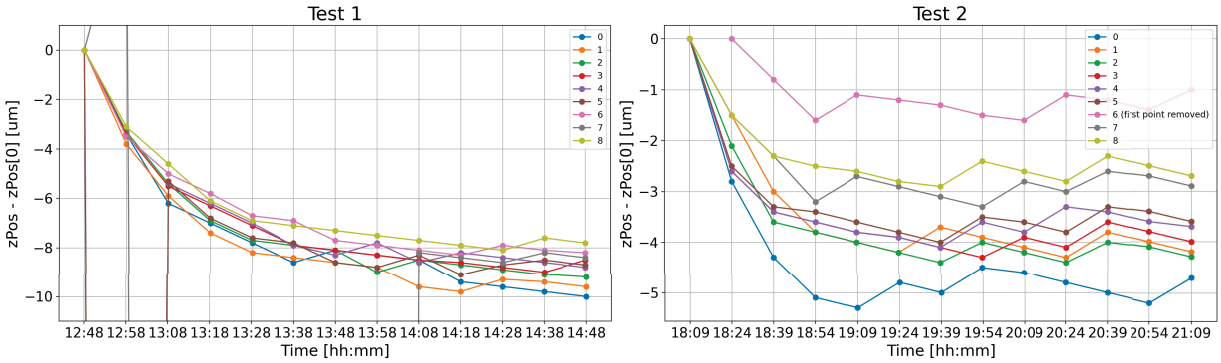

Figure 3.11: *Plots showing the change in focus over time relative to the initially found focus for 9 particles on the wafer. The only differences between the two acquisitions are the total duration (2 and 3 hours respectively) and the sampling interval (10 and 15 minutes respectively).*

In figure 3.11, plots are shown for the initial phase of acquisition of the z focus positions for two different tests, lasting 2 and 3 hours respectively. Similar results to those of the previous tests were found, with a decrease in the z focus position of 5-10μm within 2 hours for all the particles. Subsequently, for both tests, the photos taken in the second part of the acquisition are all in focus, confirming the achieved stability in the z focus positions.

However, a fixed waiting time of 2 or 3 hours is not optimal for the Virgo wafers, as it is necessary to minimize contamination while they are exposed during imaging. Therefore, a routine is implemented in the code to automatically track the focus decrease over time and start the photo acquisition as soon as the z positions stabilize. This will be presented in more detail in the next section, as part of the final version of the acquisition procedure.

3.2.7 Final Acquisition Procedure

Finally, the acquisition procedure is as follows. First, the operator searches for nine particles (one in the central area and eight evenly spaced along the edge) at a magnification of $\times$1500, and manually measures their positions (x_i, y_i) and the initial focus position z_i, where i ranges from 1 to 9. At $\times$50 magnification, a single point (x_{10}, y_{10}) and its initial focus position z_{10} are recorded. At this point, the automatic code begins [17]:

- at $\times$1500 magnification:
  - Stability check phase: measure and update the focus position for the nine particles every 15 minutes. Once the number of completed iterations reaches $n \geq 5$, after each iteration, it is verified that the last five values of the focus position for each particle are within a range of 1μm. If this condition is met, stability is considered to be reached and the code starts the real photo acquisition;
  - To determine the optimal focus position for each point (X_j, Y_j) of the grid of photos 3.2, a quadratic fit 3.1 is applied to the last 9 triplets (x_i, y_i, z_i) and then used to calculate Z_j.
  - Start taking pictures of the 315 positions and saving them as TIF files;
- at $\times$50 magnification:
  - Stability check phase: measure the focus position on the same point used manually, resulting in z'. If the new value differs less than 150μm ($|z_{10} - z'| < 150\mu m$) stability is considered achieved and proceed to take photos using z' as the focus position. If not, repeat again for a maximum of ten attempts;
  - Start taking pictures of the 63 positions and saving them as TIF files.

At $\times 1500$ magnification, a $1\mu m$ interval is chosen because during the initial stabilisation phase, the lens position typically decreases by 5 to $10\mu m$. If the difference between the last five values falls within this threshold ($1\mu m$), any possible decrease during the photo acquisition (which lasts less than 1 hour) will not significantly affect the acquisition as should not cause focusing issues. After completing the acquisition at $\times 1500$, the lens z position will have lowered. Therefore, the initial focus position z_{10} set at $\times 50$ may result in out-of-focus images and thus needs to be updated. However, if autofocus is attempted from an excessively blurry image, it may fail by moving the lens hundreds of microns further than intended. To prevent this, a threshold of $150\mu m$ has been chosen within which the new autofocus value z' must be found.

The procedure is summarized in figure 3.12. In total, it takes about 4 hours to image a wafer from the time it is taken out of the box until it can be put back into it, in particular for the phase at $\times 1500$ it takes 30-45 min to manually find the nine particles, 2 hours to reach stability, 1 hour for the actual acquisition.

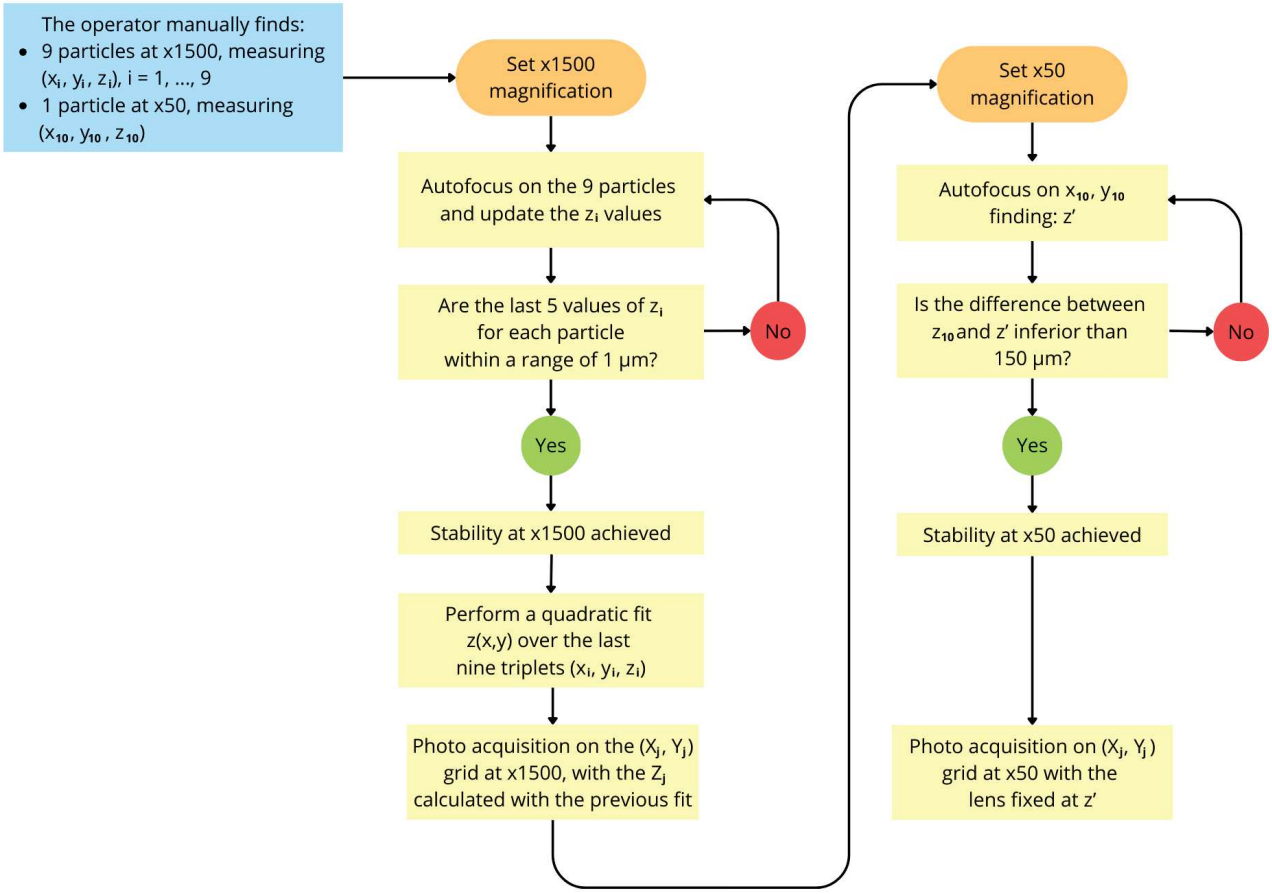

Figure 3.12: *Scheme of the final procedure for photo acquisition.*

The photographed and analysised wafers [16] refer to four environments of Virgo:

- four EQB1 samples, i.e. an in-air optical bench in the Quantum Noise Reduction system, specifically one H/V pair and two horizontal wafers with exposure times of about one month;
- two H/V pairs of samples placed in the laser bench (LB), which is part of the injection system and houses the interferometer input laser, with exposure times of approximately one month;
- one sample exposed for six months in the West Input Tower (WI), the in-vacuum tower hosting the input test masses in the west arm. Specifically, the wafers are placed on the bottom of the tower and the tower is then sealed and evacuated. Wafers are then removed just after venting.;

- four samples exposed for over a year in the Detection Tower (DET), the in-vacuum tower hosting the detection electronics used to read the signal. As for the WI tower, the wafers are placed on the bottom of the tower and the tower is then sealed and and evacuated. Wafers are then removed just after venting.

The complete list of photographed samples can be found in the appendix A. Additionally, a couple of photos, respectively at ×50 and ×1500 magnification, for the sample "LB-central-H-070323" are also provided (see B).

3.3 Wafer Analysis

After capturing the photos, the images are analyzed using a Python code developed by the Padua Virgo-ET group, which utilizes the microscope's integrated analysis software [17]. In particular, each image is first binarised: only the pixels over a certain luminosity are considered as components of particles. These informations are then processed to extrapolate the number of particles and their effective diameter (assuming that the area covered by the particle is a circle).

An example of a wafer analysis is here reported, selecting the couple of samples "LB-central-H-070323" e "LB-sidebench-V-070323": two wafers placed in the Laser Bench site on 07/03/2023 and removed on 18/04/2023, so after 42 days.

Using the number of particles and the area of the photo they cover, heatmaps of the particles density and of the percentage of area covered (PAC) can be constructed [17].

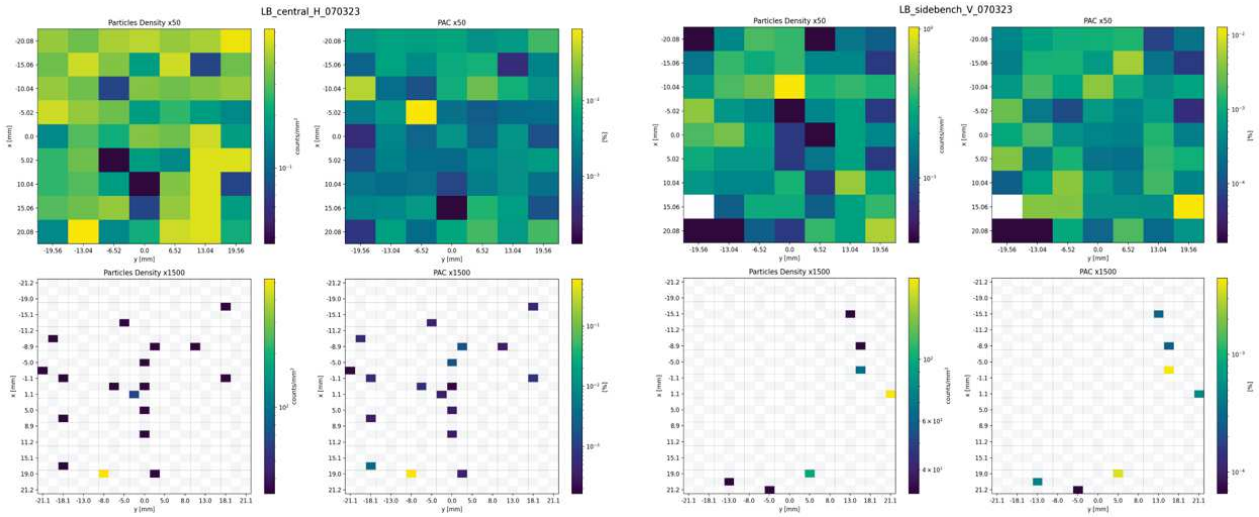

Figure 3.13: *Heatmaps of the particles density and the percentage of area covered (PAC) four the couple of samples "LB-central-H-070323" e "LB-sidebench-V-070323". Grey cells indicate that no photo was taken at that position, while white cells indicate that no particles were detected in the corresponding photos. The dimensions of the heatmap cells are not to scale. Images from [16].*

From graphs of this type, it is possible to infer some hints about the causes of particle deposition. One would expect a homogeneous distribution due to the natural and random fall of dust, whereas one would expect inhomogenueties in the spatial deposition due to human operations in the proximity of the wafers. In addition, it is evident that most of the photos taken at ×1500 are empty suggesting that for such cleanliness, imaging a larger area is necessary at this magnification level.

By looking at the size instead, histograms can be constructed with counts of particles with diameters within a certain range.

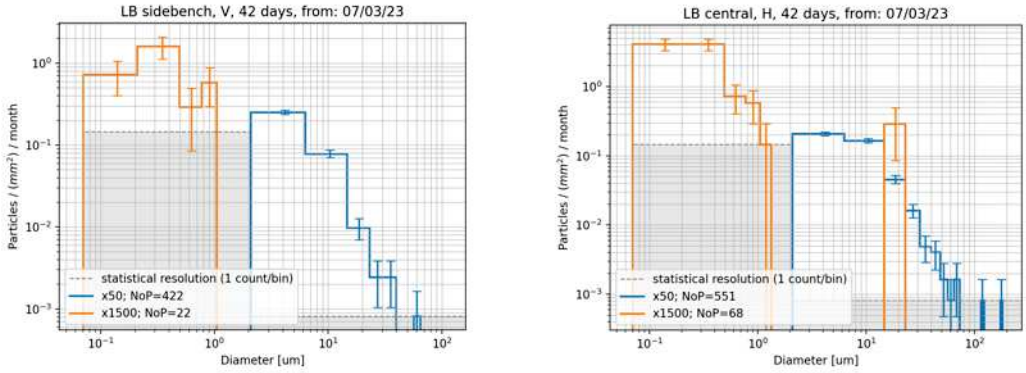

Figure 3.14: *Log - log histograms that count particles with a diamerter within a specified interval. The counts are normalised over the area covered and the exposure time of the wafers. In blue, counts for particles found in* $\times 50$ *photos; in orange,* $\times 1500$*. The error bars are associated to: the counting* ($\sqrt{N}$) *and the size of the diameter represented by the pixels, which are a function of the magnification used. Images from [16].*

Finally, looking at the total number of particles deposited on the two wafers, one can evaluate the ratio $h = NoP_V/NoP_H$. In the case of the couple analysed, it is found: $h = 43\% \pm 13\%$ [16], which is compatible with the results obtained in previous studies [15].

Chapter 4

Conclusion

Stray light is one of the main sources of low frequency noise in today's GW interferometers, and even more so in future generation interferometers such as the Einstein Telescope. The basic concepts for determining the effects of stray light from dust deposited on the wafers and thus on the optics were then presented.

With the aim of implementing a systematic acquisition procedure with the microscope, a study of the instrument's focus was carried out. In particular, having observed that the focus position z undergoes a relaxation phase of 1-2 hours during acquisition, an attempt was made to better understand and resolve this problem. The effect of temperature will need to be further investigated in the near future, as the observed decrease could be due to thermal effects on the microscope lens caused by the illumination of the microscope itself. Although the real reason for this is not yet understood, a procedure was devised that allowed the z positions to be monitored and corrected from time to time until a phase of stability was reached, when these variations were no longer significant and it was possible to start photographing the sample.

Therefore, a correct and systematic procedure for photographing the wafers used for monitoring at Virgo was found. This will now allow a large number of samples to be analysed in order to establish a clear history of dust deposition in the different environments of Virgo, both during the commissioning and the acquisition phase.

The next steps will be to photograph all the remaining wafers together with those that will continue to be exposed. The total area photographed at x1500 magnification, and therefore the statistics collected, will also be increased in order to provide more solid results. This is particularly important for environments like the towers of the Virgo main mirrors, which are very clean. In addition, from histograms of the form 3.14, the $f(D)$ can be extrapolated and the expected BSDF can be calculated using the equation 2.5. In parallel to this study, the wafers are analysed using a scatterometer, also located in the Clean Room in Padua. This makes it possible to compare the BSDF obtained from the $f(D)$ with an experimental one, thus also verifying the validity of the theoretical model.

Appendix A

Photographed wafers

The following wafers were photographed for the work carried out for this thesis [16]:

- EQB1-OnBench-H-12321;
- WI-S-H-15523;
- LB-central-H-070323;
- LB-sidebench-V-070323;
- LB-central-H-180423;
- LB-sidebench-V-180423;
- Det-E-030124;
- Det-S-030124;
- Det-W-030124;
- Det-N-030124;
- EQB1-OnBench-V-210323;
- EQB1-NearSqz-H-210323;
- EQB1-NearSQZ-H-150223.

Where the first part of the name indicates the location of the wafer (West Input Tower, Laser Bench, Detection Towers, EQB1 at the Quantum Noise Reduction site), then the orientation (H/V) is indicated and finally the date the wafer was exposed.

Appendix B

Examples of photos

Here are some photos taken during the tests and the acquisitions. Specifically: a feature focused on the plate of the microscope, one on the holder surface and then two photos at ×50 and at ×1500 for the sample "LB-central-H-070323".

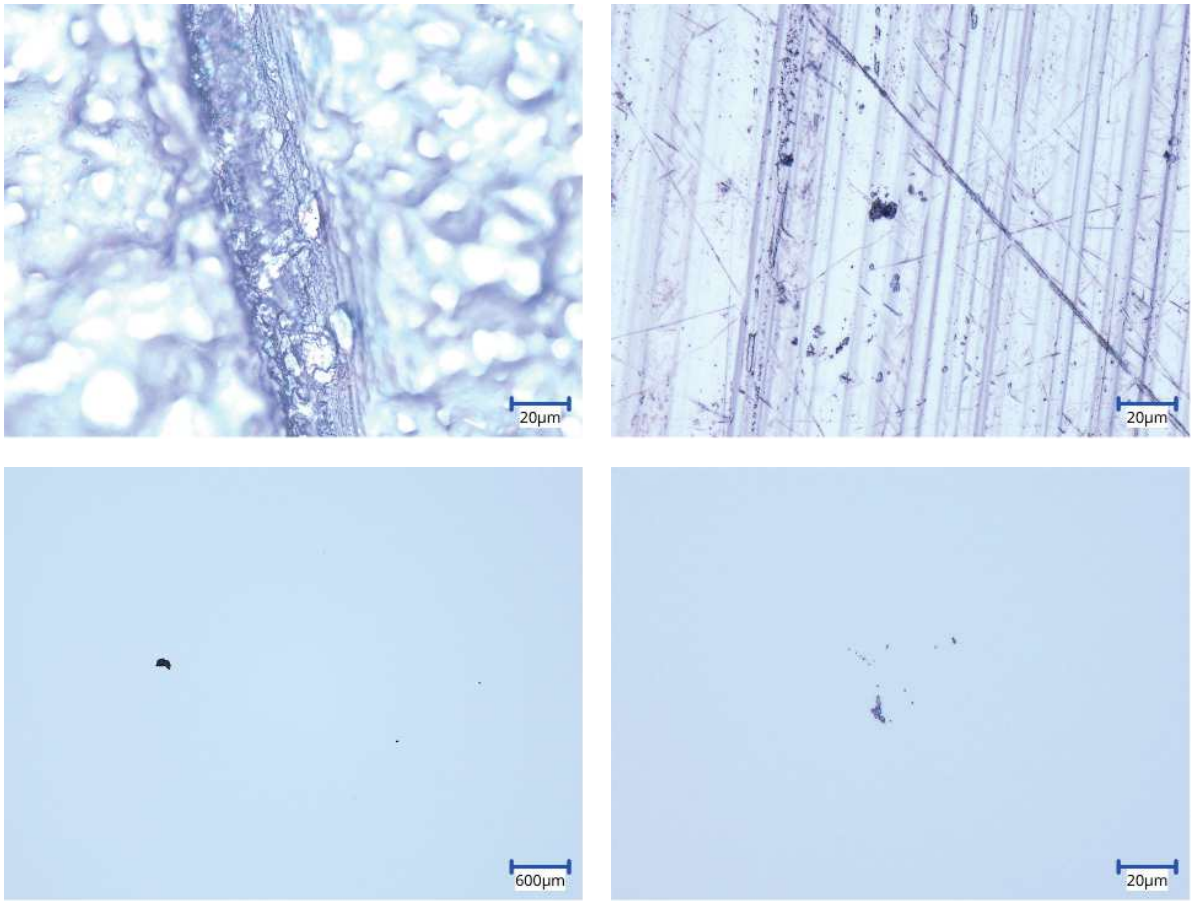

Figure B.1: *Examples of details in focus: top left a feature of the plate at* ×1500*, top right again at* ×1500*, bottom left a photo of sample 'LB-central-H-070323' at* ×50 *and bottom right a photo of the same sample at another point at* ×1500*.*

Bibliography

[1] R. Abbott et al. (LIGO Scientific, VIRGO Collaboration and KAGRA Collaboration), "GWTC-3: Compact Binary Coalescences Observed by LIGO and Virgo during the Second Part of the Third Observing Run", *Phys. Rev. Lett.*, X 13, 041039, Dec 2023.

[2] B. P. Abbot et al. (LIGO Scientific Collaboration), "Observation of gravitational waves from a binary black hole merger", *Phys. Rev. Lett.*, vol. 116, p. 061102, Feb 2016.

[3] B. P. Abbot et al. (LIGO Scientific and VIRGO Collaborations), "The basic physics of the binary black hole merger GW150914", *Phys. Rev. Lett.*, vol. 529, issue 1-2, Jan 2017, 1600209.

[4] B.D'Angelo, *Numerical Simulations of Stray Light in Virgo*, PhD Thesis, 2022.

[5] C.F. Bohren and D.R. Huffman, *Absorption and scattering of light by small particles*, Wiley science paperback series, Wiley-VCH, 1998.

[6] J.D. Buch and M.K. Barsh, *Analysis of particulate contamination buildup on surfaces*, Proc. SPIE 0777, Optical Systems Contamination: Effects, Measurement, Control, 1987.

[7] G. Favaro, *Crystallization of amorphous tantala coatings and its implication on GW interferometry*, PhD Thesis, 2022.

[8] E. Fest, *Stray Light Analysis and Control (SPIE Press PM229)*, Press Monograph, SPIE Press, 2013.

[9] A. Grado et al., *Einstein Telescope beampipe requirements*, ET-0385A-24, Issue 1, June 14, 2024.

[10] J.B. Hartle, *Gravity: An Introduction to Einstein's General Relativity*, Pearson Education Limited, 2014.

[11] S. Hemmer, L. Conti, L. Mobilia, *AIRLAB – A hands-on experience on the measurement of atmospheric particulate matter for upper secondary students*, ICERI2022 proceedings, November 2022.

[12] M.P. Hobson, G.P. Efstathiou and A.N. Lasenby, *General Relativity - An Introduction for Physicists*, Cambridge University Press, UK, 2006.

[13] International Organization for Standardization. *Cleanrooms and associated controlled environments - Part 1: Classification of air cleanliness*, ISO 14644-1:2015(E).

[14] M. Maggiore, *Gravitational Waves: Volume 1: Theory and Experiments*, Oxford University Press, USA, 2007.

[15] A. Moscatello, *Light Scattering from Dust Contamination in Gravitational-Wave Interferometric Detectors*, Master Thesis, 2022.

[16] A. Moscatello et al. *Monitoring dust contamination and estimating contributed stray light*, TDS: VIR-0514A-24, Virgo Week 05 June 2024.

[17] A. Moscatello, *Moscatello Private Communication*, 2024.

[18] Contributers: Scott Prahl, Zachary Moon, Yvan Nollet, and Jeffrey Becca. Mie-python package: https://pypi.org/project/miepython/.

[19] Virgo Collaboration, *Advanced Virgo Technical Design Report*, VIR–0128A–12, April 2012.

[20] Virgo Offical Site, *Optical Layout - Virgo*, https://www.virgo-gw.eu/science/detector/optical-layout/

[21] W. Whyte, K. Agricola and M. Derks *Airborne particle deposition in cleanrooms: Calculation of product contamination and required cleanroom class*, Clean Air and Containment Review, Issue 26, April 2016.

[22] Wikipedia, *Bidirectional Scattering Function*, https://en.wikipedia.org/wiki/Bidirectional_scattering_distribution_function.

[23] J.P. Zendri, *Course: Introduzione alla Gravitazione Relativistica*, Academic Year 2023.